Dynamic high-strain-rate mechanical behavior of microstructurally biased two-phase $TIB_2+AL_2O_3$ ceramics

Greg Kennedy and Louis Ferranti
School of Materials Science and Engineering, Georgia Institute of Technology, Atlanta, Georgia 30332-0245

Rod Russell
Institute for Advanced Technology, University of Texas, Austin, Texas 78759

Min Zhou
Woodruff School of Mechanical Engineering, Georgia Institute of Technology, Atlanta, Georgia 30332-0245

Naresh Thadhani[a)]
School of Materials Science and Engineering, Georgia Institute of Technology, Atlanta, Georgia 30332-0245

(Received 10 June 2001; accepted for publication 1 November 2001)

The dynamic high-strain-rate behavior of two-phase $TiB_2+Al_2O_3$ ceramics with biased microstructures was investigated in this study. The microstructural bias includes differences in phase (grain) size and phase distribution such that in one case a continuous (interconnected) TiB_2 network surrounds the Al_2O_3 phase (qualitatively termed ''T@A'') and in another case the TiB_2 and Al_2O_3 phases are interdispersed and uniformly intertwined with each other (qualitatively termed ''TinA''). Quantitative microscopy was used to characterize the phase size and the integral curvature which is taken as a measure of TiB_2 phase connectivity around Al_2O_3. Dynamic compression and tension (spall) properties were measured using plate impact experiments. The measurements used piezoelectric polyvinyldine fluoride stress gauges to obtain the loading profile and to determine the Hugoniot elastic limit. In addition, velocity interferometry system for any reflector interferometry was used to obtain the spall signal and the tensile dynamic strengths of the materials. Experimental results reveal that while the σ_{HEL} and the compressive strengths of $TiB_2+Al_2O_3$ ceramics are dependent on the average grain (phase) size, the tensile (spall) strength scales with the TiB_2-phase connectivity. This result suggests that the interconnected TiB_2/Al_2O_3 microstructural morphology provides a stronger impediment to failure in tension compared with the morphology with simply interdispersed phases. [DOI: 10.1063/1.1429770]

I. INTRODUCTION

The dynamic, high-strain-rate deformation behavior of materials (and consequently their ballistic performance) is dramatically influenced by their microstructural characteristics, including phase size, phase morphology, composition and texture. Such a trend has been revealed not only for steels used as heavy armor, but also for ceramics considered for lightweight armor applications.[1] In addition to their low density, ceramics exhibit superior hardness and high compressive strength that enables erosion and ''interface defeat'' of projectiles. This mechanism makes ceramics highly desirable for use as armor materials. Over the last 30 years a number of studies on ballistic performance and dynamic behavior[1–19] have been performed on various ceramics (e.g., AlN, Al_2O_3, B_4C, SiC, TiB_2, WC, ZrO_2). These studies have suggested that the desirable characteristics of ceramics that are beneficial for the defeat of projectiles include the combination of high yield strength or hardness, high tensile spall strength, high fracture toughness, high Poisson's ratio, and high coefficient of friction.[15] The properties typically measured to characterize the dynamic behavior of ceramics are the Hugoniot elastic limit (σ_{HEL}) and spall strength. In general, the spall strength is lower than the elastic limit. Materials such as TiB_2 have a spall strength that decreases with increasing impact stress and becomes negligible at the σ_{HEL}. In contrast, Al_2O_3 maintains its original spall strength even at impact stress levels that exceed the σ_{HEL}.[3]

It has been demonstrated that SiC and TiB_2 exhibit the most desirable ballistic properties based on results of experiments performed to determine the transition between interface defeat and penetration involving W projectiles.[14–16] The impact velocity for dwell/penetration transition for SiC and TiB_2 is higher than that for B_4C, in spite of the higher yield strength of the latter. This trend is consistent with the predictions from the dwell/penetration transition model[17] which accounts for damage mechanism based on the extension of mode-I wing cracks. The predictions illustrate that SiC and TiB_2 ceramics have the ability to suppress the formation of wing cracks due to plastic relaxation of preexisting flaws, while B_4C shows a brittle behavior dominated by growth of wing cracks. Brittle fracture is also expected to dominate the behavior of Al_2O_3. Measurements of shock wave profiles have also illustrated the ability of SiC and TiB_2 ceramics to undergo deformation-induced hardening,[18] which may give rise to improved ballistic properties.

Most dynamic behavior studies performed to date have focused on single-phase monolithic ceramics, although ce-

[a)]Electronic mail: naresh.thadhani@mse.gatech.edu

ramics with glassy (impurity) phases, e.g., AD85 Al_2O_3, have also been investigated. In such ceramics, the presence of intergranular oxide glass has been shown to significantly lower the tensile (spall) strength, and, therefore, the fracture resistance.[19] Dynamic behavior of ductile metal-matrix composites, e.g., Al alloys consisting of embedded ceramic particles, has been studied to a limited extent.[20] It has been shown that both the dynamic yield strength and the spall strength are reduced, in comparison to strength increases observed in particle-reinforced composite materials under quasistatic loading conditions. The composite structure acts as a mechanical energy trap due to scattering of waves from incoherent boundaries and interfaces between the matrix and reinforcement phases having dissimilar shock impedance. The high-strain-rate mechanical behavior of ceramic–ceramic composites shows a strain rate dependence significantly different from that observed in metal-matrix composites. Dynamic behavior of ceramic composites has been limited only to the study of two-phase $Al_2O_3+TiB_2$ ceramics (70/30 mass ratio). Past work on these two-phase ceramics has revealed an 80% increase in compressive strength with increasing strain rate (3.5 GPa at $10^{-4}\ s^{-1}$–5.8 GPa at $10^3\ s^{-1}$) as shown in Fig. 1(a).[21] In addition, as illustrated in Fig. 1(b), the two-phase $Al_2O_3+TiB_2$ ceramics have static and dynamic mechanical properties superior to their monolithic constituents.[21–23] The $Al_2O_3+TiB_2$ ceramics have also shown better penetration resistance than monolithic Al_2O_3, and the system in which TiB_2 is an interconnected phase surrounding Al_2O_3 has been shown to exhibit a superior ballistic performance compared with the system in which the two phases are simply uniformly interdispersed.[21,24] Micromechanical simulations have also demonstrated the effect of microstructural bias on failure resistance.[25,26] However, the influence of microstructural bias on the fundamental dynamic properties of these ceramics has not been fully established.

The objective of the present work is to characterize the high-strain-rate deformation and damage response of four types of microstructurally biased, two-phase $TiB_2+Al_2O_3$ ceramics. The microstructural bias of the four ceramics falls into two morphological categories. The first category involves a continuous (interconnected) TiB_2 network that surrounds Al_2O_3 (qualitatively termed "T@A") and the second category involves TiB_2 and Al_2O_3 phases that are interdispersed and uniformly intertwined with each other (qualitatively termed "TinA").[21] Normal plate impact experiments were used to measure the σ_{HEL} and the spall strength of the materials. The measured responses were then correlated with the microstructure morphological characteristics and the phase size scales.

II. PREPARATION AND CHARACTERIZATION OF THE TWO-PHASE CERAMICS

The two-phase $TiB_2+Al_2O_3$ ceramics were fabricated as ~80 mm diameter by 20-mm-thick disks by hot-pressing powders. The powders were produced through either self-propagating high-temperature synthesis (SHS) reactions between powder precursors ($3TiO_2+3B_2O_3+10Al=3TiB_2$

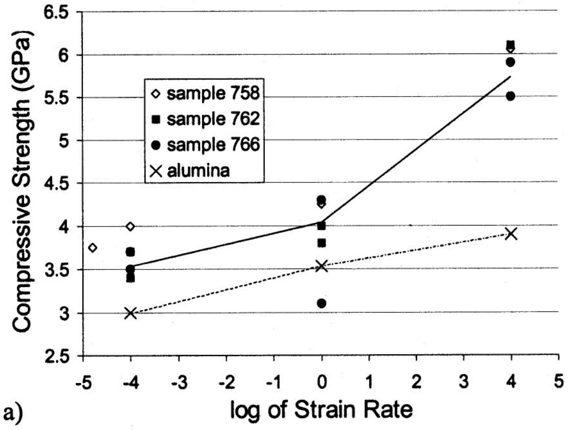

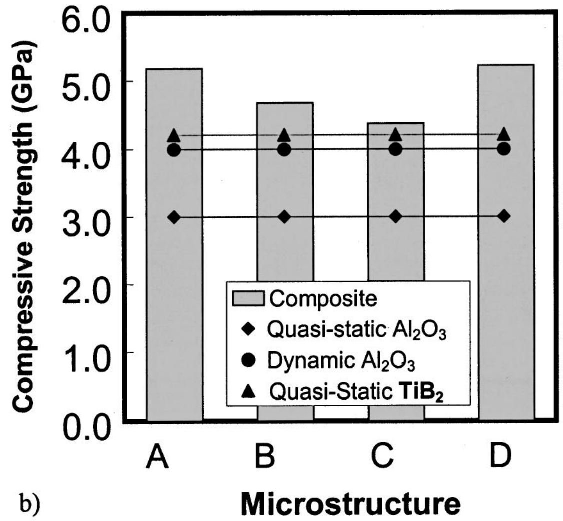

FIG. 1. (a) Strain-rate dependence of compressive strength for $Al_2O_3+TiB_2$ (solid line) in contrast to that for Al_2O_3 (dashed line) (see Ref. 23). (b) A comparison of the dynamic compressive strengths of two-phase $TiB_2+Al_2O_3$ with those of the monolithic constituents (see Ref. 23).

$+Al_2O_3$; 33:67 weight ratio), or through manual mixing (MM) of the constituents (nominally, 30 wt% TiB_2 +70 wt% Al_2O_3) which are obtained using conventional powder processing techniques. Following the SHS synthesis or manual mixing, the powders were also ball milled to generate the microstructural bias. Details of the processing approaches used for fabricating these two-phase $TiB_2+Al_2O_3$ ceramics are described elsewhere.[21,27]

Quantitative metallography[28] was performed to determine the phase size (as measured by the linear intercept length) and phase connectivity (based on measurement of integral curvature). The connectivity of a phase in a multiphase material can be related to a quantitative measurement of curvature, k, defined as the angle, $d\theta$, of a finite segment of an arc divided by the length of the arc $d\lambda$, or

$$k=d\theta/d\lambda. \tag{1}$$

Through a division of line integrals, the average curvature, k_{ave} can be calculated by dividing the angle of arc θ_A^{net} (in phase A) by total length of arc, L_A. Hence,

$$k_{ave}=\theta_A^{net}/L_A=\{\theta_A^+-\theta_A^-\}/L_A, \tag{2}$$

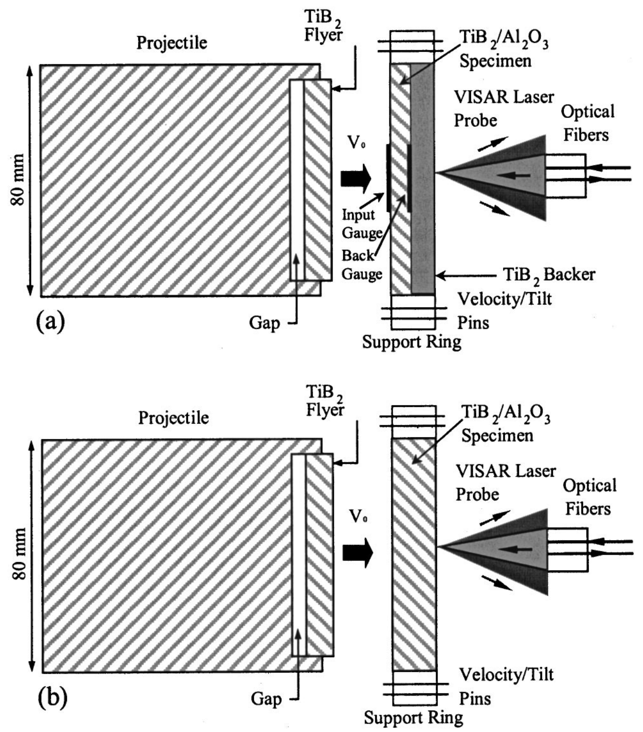

FIG. 2. Schematic illustrations of the setups used for measurements of (a) stress profiles with PVDF gauges and (b) free-surface velocity traces with VISAR interferometry.

where, θ_A^+ is angle for a convex arc and θ_A^- is angle for a concave arc in phase A. If the phases are considered as closed (as in the case of our two-phase ceramic), then the angle of the arc is 2π. Hence the above equation can be written as

$$k_{\text{ave}}=(2\pi)N_A^{\text{net}}/L_A=2\pi\{N_A^+-N_A^-\}/L_A, \tag{3}$$

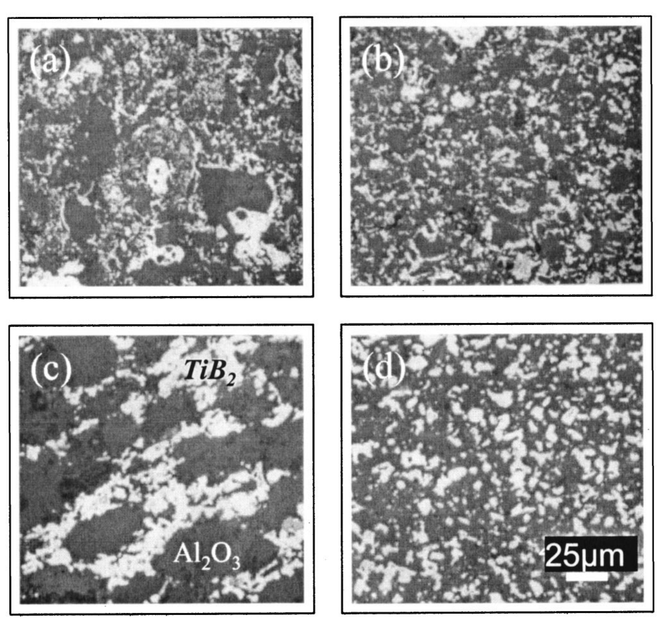

FIG. 3. Optical micrographs of two-phase ceramics (TiB_2 white and Al_2O_3 dark phase). (a) Sample A, SHS, T@A microstructure, (b) sample B, SHS, TinA microstructure, (c) sample C, MM, T@A microstructure, and (d) sample D, MM, TinA microstructure.

TABLE I. Measured average values of integral curvature, and sizes of constituent phases.

Microstructure type	Average integral curvature (μm^{-1})	TiB_2 phase size (μm)	Al_2O_3 phase size (μm)
A	-0.316 ± 0.022	7.0	10.4
B	-0.476 ± 0.046	6.2	9.1
C	-0.074 ± 0.028	8.7	25.1
D	-0.375 ± 0.031	7.9	12.3

where, N_A^{net}, N_A^+, and N_A^- are the net, positive, and negative numbers of loops of phase A. The length of the arc, L_A, of a closed loop is the perimeter and can be related to the mean linear intercept length L using $L_A=(\pi/2)(1/L)$. The average integral curvature of phase A can then be expressed as

$$k_{\text{ave}}=4.N_A^{\text{net}}L. \tag{4}$$

In the present work, the average integral curvature values were determined using Eq. (4). The mean linear intercept length L and the number of net loops of "A" (or TiB_2) phase around the "B" (or Al_2O_3,) phase were determined using IMAGEPRO-PLUS, a commercial software package (product of Media Cybernetics). To account for anisotropy effects, the analysis was performed on at least ten micrographs of both planar and cross-sectional surfaces. However, the differences due to anisotropy were found to be in the range of the standard deviation.[29]

The impact experiments used an 80-mm-diam, single-stage gas gun. Measurements of the σ_{HEL} and the shock wave speeds under dynamic compression were obtained from stress profiles recorded using polyvinyldine floride (PVDF) stress gauges. As shown in Fig. 2(a), a TiB_2 flyer plate backed by an air gap and mounted at the head of an aluminum projectile, was used to impact the target assembly consisting of ~3-mm-thick ceramic sample backed by a TiB_2 backer plate. Impact experiments were conducted at a nominal velocity of ~0.750 km/s (~15 GPa nominal impact stress) to ensure shock loading of samples under similar conditions. The impact velocity was measured using arrival time pins. One PVDF gauge package was placed at the impact surface and another was placed between the sample and TiB_2

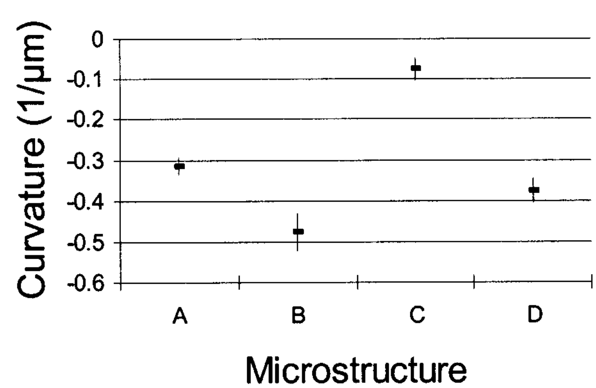

FIG. 4. Plot comparing the average integral curvature values of the TiB_2 $+Al_2O_3$ ceramic samples of four different types of microstructures. Note that the TiB_2 phase connectivity is greater in sample A than in sample B, and likewise in sample C than in sample D.

TABLE II. Measured values of density, elastic wave velocity, and Young's and shear moduli of the four types of microstructurally biased ceramic samples.

Sample type	Density (g/cm^3; %TD)	Long. vel (km/s)	Shear vel. (km/s)	Young's mod (GPa)	Shear mod (GPa)
A	4.095; 99.4%	11.114	6.477	505.8	171.8
B	3.939; 95.6%	10.336	6.145	420.8	148.7
C	4.108; 99.7%	10.796	6.527	478.8	175.0
D	4.083; 99.1%	10.773	6.523	473.9	173.7
TiB_2[a]	4.509	10.790	7.43	524.9	248.9
Al_2O_3[a]	3.55	9.280	5.47	306.2	106.4

[a]Values of TiB_2 and Al_2O_3 are from D. E. Grady, Sandia Report No. SAND-91-014, UC-704, 1991.

backer plate. The experimental setup was designed such that a planar-parallel shock wave propagates through the target and the input and propagated stress profiles are measured with little interference from radial reflected waves. The PVDF gauges were connected to current viewing resistors to allow current versus time data acquisition with a 1 GHz frequency oscilloscope. The current versus time data were then numerically integrated to yield stress versus time profiles for the impact and propagated wave gauges. The arrival time at the respective gauges was taken as the travel time through the sample thickness, from which the shock wave speed was determined.

Figure 2(b) shows the experimental setup, illustrating the target sample (without any backer) being impacted by a projectile consisting of a 4140 steel (or silicon carbide) flyer plate and an aluminum sabot. An air gap exists between the flyer plate and the sabot to allow full unloading required for the spall strength measurements. All sample surfaces were lapped for flatness and parallelism. The ceramic targets were polished with 5 μm diamond paste to ensure reflectivity required by the velocity interferometer system for any reflector (VISAR) beam. The time-resolved longitudinal motion of the sample free surface was measured in the form of interference fringes with a Valyn VISAR and recorded on a digital oscilloscope. The interference fringes were then converted to time-resolved history of particle velocity.

III. RESULTS AND DISCUSSIONS

A. Microstructural characterization

Optical micrographs of the four types of microstructurally biased samples studied are shown in Figs. 3(a)–3(d). The micrographs correspond to sample A made by the SHS process with TiB_2 surrounding Al_2O_3 (T@A); sample B also made by SHS with intermixed TiB_2 and Al_2O_3 (TinA) phases; sample C made by MM with TiB_2 surrounding Al_2O_3 (T@A); and sample D made by MM with intermixed TiB_2 and Al_2O_3 (TinA) phases. It should be noted that the samples do not reveal 100% microstructural bias, i.e., while the micrographs of samples A and C generally illustrate a nearly continuous (interconnected) TiB_2 phase surrounding Al_2O_3, regions where the converse is true are also present. Likewise, samples B and D show not only an intermixed structure but also the continuous phase microstructures.

Table I lists the values of average integral curvature and the average size of TiB_2 and Al_2O_3 phases. In general, the average sizes of TiB_2 and Al_2O_3 phases in both SHS samples (A and B) are smaller than those in the manually mixed samples (C and D), with sample C showing the largest size for both constituents. Sample C also represents the microstructure with the highest value of connectivity for TiB_2, as illustrated in Fig. 4. All samples, in fact, show a negative curvature, since, within a given area of measurement, the *number* of loops around smaller particles is greater than that surrounding the larger particles. This skews the average integral curvature towards negative values. Nevertheless, the measured values provide a quantitative measure of the microstructural bias on the basis of phase connectivity, and illustrate that the connectivity of TiB_2 phase is greater in sample A than in sample B, and likewise in sample C than in sample D. The grain size of the respective phases also shows a similar trend, with sample A being coarser than sample B, and sample C being coarser than sample D.

B. Characterization of elastic properties

The elastic properties of the ceramics were characterized using an Ultran Laboratories ultrasonic test apparatus. The setup allows determination of the longitudinal and shear wave velocities from which the elastic moduli are obtained using densities measured on individual samples by the Archemedean method. Table II lists the results of elastic wave velocity measurements and corresponding Young's and shear moduli. It can be seen that the moduli of the various ceramic samples are relatively similar except in the case of sample B, which has ~4.4% porosity.

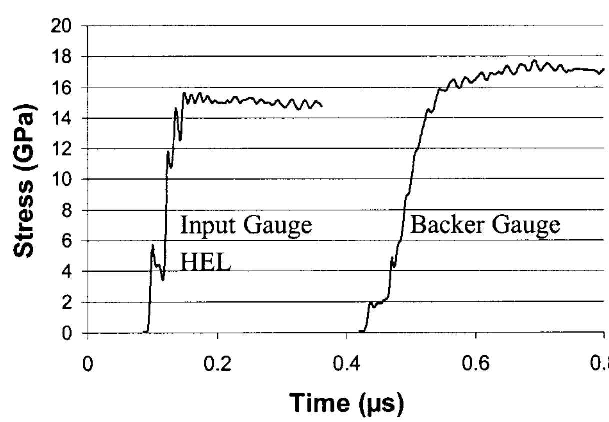

FIG. 5. Typical input and backer gauges stress profiles (sample B) obtained from Expt. 9916.

TABLE IV. Loading conditions and summary of results of spall experiments.

Sample type and expt. No.	Flyer plate material	Flyer & target th. (mm)	Target density (%TMD)	Impact velocity (m/s)	Input stress (GPa)	Spall strength (GPa)
A-0005	4140 steel	2.66/16.22	98.8%	495	7.9	0.320
A-0007	4140 steel	2.66/16.20	98.8%	237	3.7	0.320
A-0008	4140 steel	2.66/7.99	98.8%	758	11.8	0.160
C-9925	SiC	4.30/7.54	99.7%	244	3.8	0.311
D-9926	SiC	4.77/7.10	99.1%	239	3.8	0.222

thick AISI 4140 steel flyer plate. The velocity traces reveal a spall signal (velocity decrease, ΔU_{fs}) which was used to compute the spall strength ($\sigma_{\mathrm{spall}} = 1/2\rho_0 C_0 \Delta U_{\mathrm{fs}}$.) As shown in Table IV, the spall strength for sample A is 0.320 MPa at input stresses of 3.7 and 7.9 GPa. However, with input stress increasing to 11.8 GPa, the spall strength decreases to 0.160 GPa. It can be seen that while the spall strength decreases with increasing input stress, the two-phase $TiB_2 + Al_2O_3$ ceramic maintains non-negligible spall strength even at input stresses exceeding the Hugoniot elastic limit (6.2 ± 3.4 GPa).

Tensile spall experiments were also performed on samples of microstructures C and D, at an input stress of ~3.8 GPa. Figure 7 shows the free velocity traces for these samples. A spall strength of 0.311 GPa for sample C and 0.222 GPa for sample D was observed. A comparison of spall test results between sample C and sample D shows that the latter sample with dispersed microstructure has a lower spall strength, while the microstructure with interconnected TiB_2 has a higher spall strength, even though sample D has a smaller phase size. The measured high value of spall strength of the two-phase ceramic is similar to the published spall strength of TiB_2 (0.33 GPa) but lower than that of Al_2O_3 (0.45 GPa).

IV. DISCUSSION AND SUMMARY OF RESULTS

The two-phase $TiB_2 + Al_2O_3$ ceramics, made either by the SHS or mechanical milling methods, reveal differences in microstructure which qualitatively show TiB_2 as a continuous (interconnected) phase surrounding Al_2O_3 (T@A), or TiB_2 and Al_2O_3 intermixed with each other (TinA). Quantitative microscopy analysis based on the measurement of the integral curvature showed that the samples investigated do not exhibit 100% microstructural bias. However, the overall trend of the influence of microstructural bias emerging from the results of experiments performed to date illustrates that the dynamic yield strength and the σ_{HEL} are more dominantly dependent on the phase size. Sample C prepared by manual mixing and having the largest phase (grain) size shows the lowest values in contrast to the other samples of similar (~99%) density. In contrast, the tensile spall strength appears to scale with the continuity of the TiB_2 phase. Sample C, which has the most interconnected TiB_2 phase, has the highest value of the tensile spall strength.

The results therefore, illustrate that while the Hugoniot elastic limit and the dynamic compressive yield strength of $Al_2O_3 + TiB_2$ are dependent on the average grain (phase) size, the tensile spall strength scales with the TiB_2-phase connectivity, and less so with the average phase size. It is possible that the interconnected phase morphology is more effective in impeding initiation and progression of fracture under tensile conditions. If so, TiB_2 as an interconnected phase has the ability to suppress and relax the cracks formed in Al_2O_3. Alternatively, it is also possible that in the two-phase ceramic with the microstructure containing dispersed Al_2O_3 and TiB_2 phases, the mechanical energy trapping due to scattering of waves from incoherent boundaries and interfaces results in the lowering of the tensile (spall) strength. Further work is currently in progress to more clearly delineate the effects of interconnected versus dispersed TiB_2 phase, and to eventually fabricate two-phase $Al_2O_3 + TiB_2$ ceramics with the microstructural bias that yields the most optimal dynamic properties.

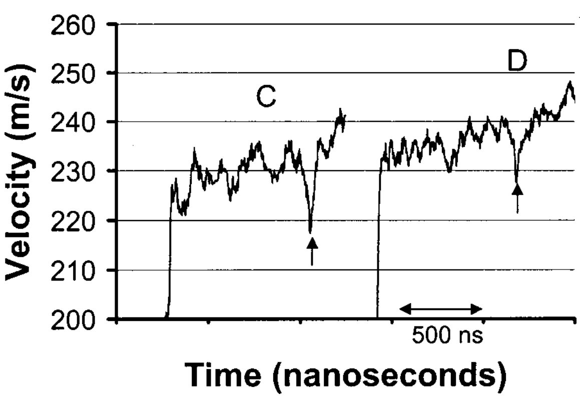

FIG. 7. Free-surface velocity traces obtained for samples C and D, at similar loading conditions.

ACKNOWLEDGMENTS

Funding for this research was provided by the U.S. Army Research Office, under Grant No. DAAG55-98-1-0454 (Dr. David Stepp program monitor). The authors thank Dr. K. V. Logan for providing the samples being investigated in the present work, and also appreciate her valuable discussions and comments.

[1] D. J. Viechnicki, M. L. Slavin, and M. I. Kliman, Ceram. Bull. **70**, 1035 (1991).
[2] D. A. Shockey, A. H. Marchand, S. R. Skaggs, G. E. Cort, M. W. Burkett, and R. Parker, Int. J. Impact Eng. **9**, 263 (1990).
[3] D. E. Grady, Sandia National Laboratories Report No. SAND91-0147, 1991.
[4] D. E. Grady and J. L. Wise, Sandia National Laboratories Report No. SAND93-0610, 1993.

[5] D. P. Dandekar and D. C. Benfanti, J. Appl. Phys. **73**, 673 (1993).
[6] D. E. Grady, Sandia National Laboratories Report No. SAND94-3266, 1995.
[7] D. L. Orphal, R. R. Franzen, A. C. Charters, T. L. Menna, and A. J. Piekutowski, Int. J. Impact Eng. **19**, 15 (1997).
[8] R. Feng, Y. M. Gupta, and M. K. Wong, J. Appl. Phys. **82**, 2845 (1997).
[9] J. Lankford, W. W. Predebon, J. M. Staehler, G. Subhash, B. J. Plekta, and C. E. Anderson, Mech. Mater. **29**, 205 (1998).
[10] G. R. Johnson and T. J. Holmquist, J. Appl. Phys. **85**, 8060 (1999).
[11] D. P. Dandekar and P. I. Bartkowski, in *Fundamental Issues and Applications of Shock Wave and High Strain Rate Phenomena*, edited by K. P. Staudhammer, L. E. Murr, and M. A. Meyers (Elsevier, New York, (2001), pp. 71–77).
[12] G. E. Hauver, P. H. Netherwood, R. F. Blenck, and L. K. Kecskes, 19th Army Science Conference, Florida, June 20–24, 1994.
[13] H. D. Espinosa, N. S. Brar, G. Yuan, Y. Xu, and V. Arrietta, Int. J. Solids Struct. **37**, 4893 (2000).
[14] F. I. Grace, in Ref. 11, pp. 421–428.
[15] J. C. LaSalvia, E. J. Horwarth, E. Rapacki, C. James Shih, and M. A. Meyers, in Ref. 11, pp. 437–446.
[16] P. Lundberg, R. Renstrom, and B. Lundberg, Int. J. Impact Eng. **24**, 259 (2000).
[17] H. Horii and S. Nemat-Nasser, Philos. Trans. R. Soc. London, Ser. A **319**, 337 (1986).
[18] D. E. Grady, Mech. Mater. **29**, 181 (1998).
[19] S. Sundaram and R. J. Clifton, Mech. Mater. **29**, 233 (1997).
[20] J. N. Johnson, R. S. Hixon, and G. T. Gray, J. Appl. Phys. **76**, 5706 (1994).
[21] K. V. Logan, Ph.D. dissertation, Georgia Institute of Technology, 1993.
[22] A. Keller, M.S. thesis, Georgia Tech., 2000.
[23] A. Keller, G. Kennedy, L. Ferranti, M. Zhou, and N. Thadhani, in Proceedings of the Fourth International Symposium on Impact Engineering, Kumamoto, Japan, July 2001 (to be published).
[24] G. Gilde, J. W. Adams, M. Burkins, M. Motyka, P. J. Patel, E. Chin M. Sutaria, M. Rigali, and L. Prokurat Franks, presented at the 25th Annual Cocoa Beach Conference of the American Ceramic Society, Jan. 23–28, 2001.
[25] J. Zhai and M. Zhou, Int. J. Fract. **101**, 161 (2000).
[26] M. Zhou and J. Zhai, presented at the American Ceramic Society 102nd Annual Meeting & Exposition, St. Louis, MO, April 30–May 3, 2000.
[27] K. V. Logan, US Patent No. 5,141,900 (25 August, 1992).
[28] E. E. Underwood, *Quantitative Stereology* (Addison–Wesley, Reading, MA, 1970).
[29] G. Kennedy, J. Zhai, R. Russel, M. Zhou, and N. N. Thadhani, presented at the 24th Annual International Conference on advanced Ceramics and Composites, Cocoa Beach, FL, Jan 23–28, 2001.